crystals

MDPI

Article

Precipitation of Carbides in $FeCr_{15}Al_x$ Alloys with Different Heat Treatments Studied by Internal Friction Technique

Yan Sun [1,2], Yuankai Jiang [1,2], Hongquan Zhang [1,2], Xinggang Wang [3], Weibin Jiang [2,*] and Meng Sun [2,*]

[1] Institutes of Physical Science and Information Technology, Anhui University, Hefei 230601, China
[2] Key Laboratory of Materials Physics, Institute of Solid State Physics (HFIPS), Chinese Academy of Sciences, Hefei 230031, China
[3] Shandong Key Laboratory of Advanced Structural Materials Genome Engineering, Yantai University, Yantai 264005, China
* Correspondence: wbjiang@issp.ac.cn (W.J.); mengsun@issp.ac.cn (M.S.)

Abstract

Fe-Cr-based alloys have great potential for large-scale vibration and noise reduction. Appropriate heat treatment is important for improving their damping capacity. However, $M_{23}C_6$-type carbides are common grain boundary precipitates during the heat treatment process, and can affect both damping behavior and mechanical properties. In this work, the effects of Al content and annealing temperature on the microstructure, internal friction (IF), room temperature damping capacity, and tensile properties of Fe-15Cr-(0-4) Al (wt.%) alloys were investigated. When annealed at 800 °C, Al addition can suppress grain boundary precipitation, and no obvious intergranular precipitates were observed in the S2Al-S4Al alloys. The ultimate tensile strength also increased with Al addition, and the S4Al alloy exhibited a 34% higher strength than S0Al while retaining an elongation of 47.7%. The maximum damping value increased with Al addition. However, annealing at 1000 °C promoted continuous grain boundary carbide formation and reduced the elongation. These results indicate that the S4Al alloy annealed at 800 °C provides a favorable balance between damping capacity and mechanical properties.

Keywords: damping; internal friction; $M_{23}C_6$ precipitates; Fe-Cr alloys; grain boundary relaxation

1. Introduction

Fe-Cr-based alloys combine high damping capacity with good corrosion resistance, mechanical properties, and relatively low cost, rendering them promising candidates for structural applications in vibration and noise reduction, as well as nuclear components such as cladding and piping systems [1–3]. The damping mechanism of these alloys is mainly associated with the stress-assisted irreversible motion of 90° magnetic domain walls and leads to highly efficient energy dissipation [1,2,4–6]. Although dislocations, grain boundaries, internal stress, and various precipitates can all hinder domain wall motion, high-temperature heat treatment can often be used to reduce defect density and residual stress, thereby lowering the resistance to domain wall motion and improving damping performance [2,6–8].

However, excessively high-temperature treatment accelerates the capture and transport of interstitial atoms (such as C) and substitutional solute atoms (such as Cr) by grain boundaries, which act as high-energy sinks. As a result, grain boundary segregation and precipitation occur more easily, which can impair the mechanical properties and corrosion

Check for updates

Academic Editor: Alla S. Sologubenko

Received: 29 March 2026
Revised: 29 April 2026
Accepted: 2 May 2026
Published: 11 May 2026

Copyright: © 2026 by the authors. Licensee MDPI, Basel, Switzerland. This article is an open access article distributed under the terms and conditions of the Creative Commons Attribution (CC BY) license.

resistance of the alloys [9–16]. In Fe-Cr-based alloys and related stainless steel systems, one of the most common intergranular precipitates after heat treatment is the Cr-rich $M_{23}C_6$ carbide. Because grain boundaries have a higher defect density and serve as fast diffusion pathways, carbide nucleation and growth are preferentially promoted at these sites [13,14,17,18]. In situ TEM studies have shown that fine $M_{23}C_6$ particles initially form near grain boundaries with specific orientation relationships, followed by coalescence and gradual evolution into film-like or continuous networks. At the same time, asymmetric Cr-depleted zones appear near the grain boundaries [12,14]. When these precipitates become chain-like or form a continuous network along grain boundaries, grain boundary weakening often occurs. Thus, the toughness of the alloy decreases markedly, and sensitivity to intergranular corrosion increases significantly [9–12,15,19,20]. More importantly, in Fe-Cr-based damping alloys, grain boundary precipitates affect not only mechanical properties and corrosion resistance, but also interface-related relaxation and magnetic domain wall motion through second-phase pinning. Previous studies have shown that the more grain boundary precipitates, and the higher the Cr enrichment in them, the worse the damping capacity becomes [7,21]. Therefore, controlling the tendency of grain boundary $M_{23}C_6$ to become continuous and form a network is one of the key ways to achieve a trade-off among damping performance, structural reliability, and corrosion resistance.

Compared with the heat treatment approach, element alloying offers another way to ease this conflict. Previous studies have shown that adding a proper amount of Al to Fe-Cr alloys, such as $\leq$4 wt.%, can improve damping capacity [2,5]. Studies on interstitial atom relaxation (Snoek-type behavior) and atomistic simulations generally indicate that Al increases the activation parameters for C atom diffusion and introduces a clear kinetic trapping effect. As a result, the effective diffusion of carbon in body-centered cubic iron is reduced [22–26]. This suggests that Al may lower the effective diffusion of carbon toward grain boundaries, delay the nucleation, growth, and continuous development of $M_{23}C_6$ in grain boundaries, and thus improve both damping performance and structural reliability. However, these studies have not clarified the coupled effects of Al content and annealing temperature on grain boundary $M_{23}C_6$ precipitation in Fe-Cr-Al damping alloys. In particular, the relationship among Al addition, heat treatment, $M_{23}C_6$ precipitation, internal-friction response, damping capacity, and mechanical properties remains unclear. Therefore, the present work aims to clarify how Al addition and annealing temperature affect grain boundary $M_{23}C_6$ precipitation, and how this precipitation behavior influences the damping and mechanical properties of Fe-15Cr-xAl alloys.

Internal friction (IF) represents the mechanical loss caused by energy dissipation inside a material during cyclic loading. In mechanical spectroscopy, IF is commonly expressed by the phase lag, tan φ, between an applied periodic stress and the resulting strain [27]. The IF-temperature spectrum provides a nondestructive way to detect thermally activated processes at the atomic level, and it is especially sensitive to relaxation processes associated with phase transitions and grain boundary sliding. Studies have shown that the IF peak height and peak temperature of the grain boundary relaxation peak are affected by microstructural defects at grain boundaries [27–31]. In this work, low-carbon ferritic Fe-Cr-based alloys were selected as a model system. By varying the Al content and annealing temperature of Fe-Cr-based damping alloys, this study investigated the microstructure, the temperature-dependent IF behavior, the damping performance, and the mechanical properties. Particular attention was paid to how Al content and annealing temperature influence the precipitation of grain boundary $M_{23}C_6$, and to how such precipitation affects the temperature-dependent IF behavior, damping performance, and mechanical properties of the alloys.

2. Materials and Experimental Procedures

2.1. Materials Preparation

Ingots weighing about 80 g and having a nominal composition of Fe-15Cr-xAl (x = 0, 1, 2, 3, 4 wt.%) were prepared by a vacuum induction furnace using pure Fe (99.99%), pure Cr (99.99%) and pure Al (99.99%) under an Ar atmosphere. All ingots were homogenized at 1200 °C for 2 h under an Ar atmosphere. The homogenized ingots were subjected to a warm rolling process at 700 °C to obtain plates with a final thickness of 3 mm. The total reduction in plate thickness was about 70%. Finally, parts of each sample were annealed at 800 °C for 1 h under an Ar atmosphere, followed by furnace cooling to room temperature. In addition, parts of the S0Al and S4Al specimens were further annealed at 900 °C and 1000 °C for 1 h, followed by furnace cooling to room temperature.

For convenience, these five alloy ingots are referred to as S0Al, S1Al, S2Al, S3Al and S4Al according to their nominal compositions. It should be noted that the alloy labels S0Al–S4Al are based on the nominal Al contents. The main chemical compositions of the five homogenized alloys measured by an electrical discharge direct reading spectrometer are shown in Table 1. It is worth noting that the measured Al content of S4Al is 3.097 ± 0.016 wt.%, which is lower than the nominal value and may be related to Al evaporation during the melting process. The carbon content for all five alloys was below 0.003 wt.%.

Table 1. Chemical compositions of the Fe-15Cr-xAl (x = 0, 1, 2, 3, 4 wt.%) alloys measured by an electrical discharge direct reading spectrometer.

Alloys	Fe (wt.%)	Cr (wt.%)	Al (wt.%)	C (wt.%)
S0Al	Bal.	14.72 ± 0.015	0.003 ± 0.003	<0.003
S1Al	Bal.	14.953 ± 0.073	1.172 ± 0.013	<0.003
S2Al	Bal.	14.645 ± 0.039	1.926 ± 0.014	<0.003
S3Al	Bal.	14.811 ± 0.055	2.536 ± 0.017	<0.003
S4Al	Bal.	14.677 ± 0.032	3.097 ± 0.016	<0.003

2.2. Measurements of IF and Tensile Properties

Damping properties were tested in a computer-controlled automatic inverted torsional pendulum (MFIFA, Hefei, China) using the forced vibration method. $Q^{-1} = \tan \varphi$ denotes the damping properties of the material, where φ denotes the phase lag between the applied cyclic stress ($\sigma = \sigma_0 \cos(\omega t)$) and the strain produced by the stress ($\varepsilon = \varepsilon_0 \cos(\omega t + \varphi)$). To characterize the temperature-dependent damping behavior, the samples with dimensions of about 30 × 2 × 1.2 mm^3 were heated continuously to 800 °C at a rate of 3 °C/min. The samples were then held at 800 °C for 10 min and then in situ cooled to room temperature in the furnace. In each test cycle, four excitation frequencies (0.5, 1, 2 and 4 Hz) were selected and the torsional strain amplitude was maintained at 2×10^{-5}. The amplitude-dependent IF behavior was measured at room temperature at a frequency of 1 Hz over a strain-amplitude range of 5×10^{-5} to 1×10^{-3}.

The tensile specimens were dog-bone-shaped samples with a gauge length of 5 mm and an effective cross-sectional area of 1.5 × 0.75 mm^2. Room temperature tensile tests were conducted using an Instron-5967 machine at a strain rate of 1×10^{-3} s^{-1}.

2.3. Microstructure Characterization

The microstructures of the alloys were characterized using a field-emission scanning electron microscope (FE-SEM, SU 8000, HITACHI, Tokyo, Japan) and electron backscatter diffraction (EBSD, Aztec X-Max 80, Oxford, UK). Samples for SEM and EBSD were prepared by standard metallographic grinding and mechanical polishing procedures, and

electropolished in a mixed solution of 90% glacial acetic acid and 10% perchloric acid at ~30 V for 60 s to remove the surface layer damaged by mechanical polishing. To observe the grain boundary precipitates under a scanning electron microscope (SEM), the samples were etched using a mixed solution of 2 g $FeCl_3 \cdot 6H_2O$, 15 mL HCl, and 35 mL ethanol for 10–15 s. The TEM samples were milled to a thickness of 40–60 μm and further processed through ion milling. Transmission electron microscopy (TEM) and scanning transmission electron microscopy (STEM) analyses were performed using an FEI Talos F200X microscope (FEI Talos F200X, Corvallis, OR, USA) equipped with a Super-X™ EDS detector operated at an accelerating voltage of 200 kV. TEM-EDS spectra were acquired from the grain-boundary precipitates to evaluate their chemical characteristics. The EDS data were processed using the Velox (3.14.0.1245-07b70aaf4c) software. Considering the limited quantitative accuracy of nanoscale EDS analysis, the elemental concentrations are reported to the nearest 1 at.%.

3. Results and Discussion

3.1. Microstructure Characterization of Alloys

Figure 1 shows the grain structure of the S0Al and S4Al alloys after annealing at 800 °C, 900 °C, and 1000 °C for 1 h. After annealing, both alloys exhibited a clear equiaxed grain structure and retained the BCC crystal structure. And as the annealing temperature rises, the grain size increases rapidly. The average grain size across multiple regions of the alloy was measured using the equivalent circle diameter method. It should be noted that there are inherent errors in the statistical analysis. Table 2 summarizes the average grain size in the S0Al and S4Al alloys after annealing at different temperatures. It is worth noting that, under the same heat treatment conditions, the S0Al alloy shows a larger average grain size than the S4Al alloy, especially at low-temperature heat treatment, where the average grain size of S0Al is nearly twice that of S4Al. However, after heat treatment at 1000 °C for 1 h, with rapid grain growth, the average grain sizes of the two samples are tended to be consistent. This result indicates that the addition of Al can refine the grains, and the effect is more pronounced at lower temperatures.

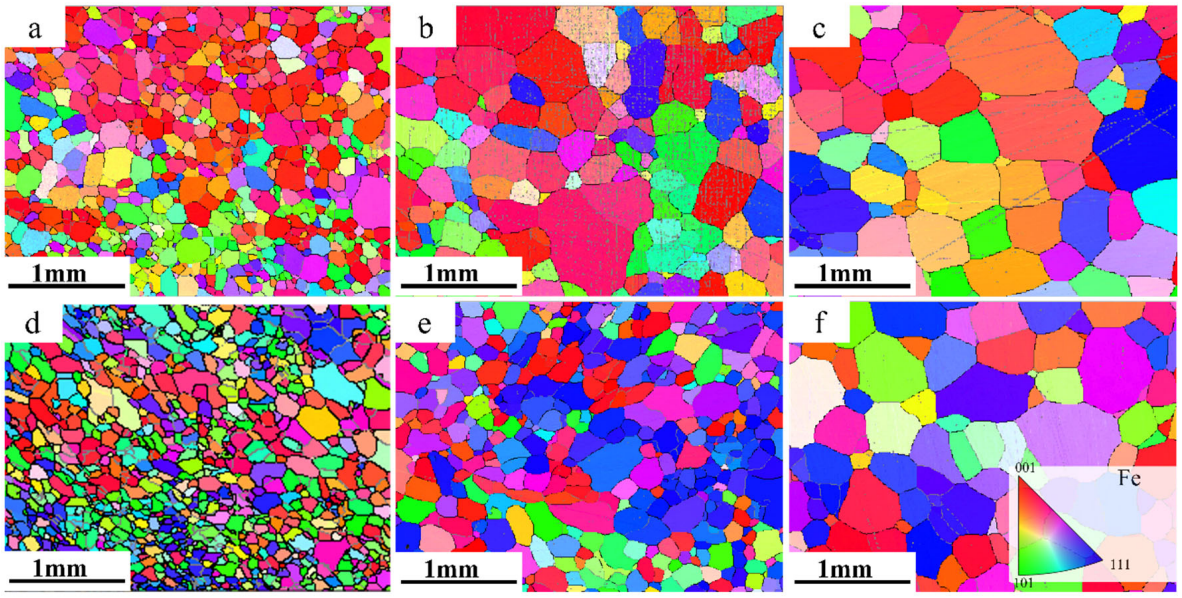

Figure 1. EBSD maps of the S0Al samples annealed for 1 h at (**a**) 800 °C, (**b**) 900 °C, and (**c**) 1000 °C, and the S4Al samples annealed for 1 h at (**d**) 800 °C, (**e**) 900 °C, and (**f**) 1000 °C. The inset shows an IPF map.

Table 2. Average grain size of the S0Al and S4Al samples after heat treatment at 800 °C, 900 °C, and 1000 °C for 1 h, respectively.

Temperature	**800 °C**		**900 °C**		**1000 °C**	
Sample	**S0Al**	**S4Al**	**S0Al**	**S4Al**	**S0Al**	**S4Al**
Average grain size (μm)	144.66 ± 67.08	87.47 ± 37.78	283.5 ± 174.4	181.93 ± 95.76	379.28 ± 203.63	348.17 ± 212.85

The grain boundary microstructures of the S0Al-S4Al alloys after annealing at 800 °C for 1 h are shown in Figure 2. After etching in the corrosive solution for 10–15 s, the S0Al alloy exhibited obvious grain boundary grooves, and continuously distributed film-like precipitates were observed along the grain boundary (see the inset in Figure 2a). In the S1Al alloy, grain boundary groove appeared only along part of the grain boundaries, and only a small number of film-like precipitates were observed. In contrast, no obvious grain boundary grooves were found in the S2Al-S4Al alloys, and the grain boundaries remained clean, with no visible precipitates. The SEM image of the grain boundary precipitates in the S0Al alloy and the corresponding EDS line scan analysis are shown in Figure 3. Compared with the matrix, Cr and C are enriched at the grain boundary, confirming that the grain boundary precipitates are Cr-rich MC-type carbides. These results indicate that the addition of Al can effectively suppress the formation of MC-type carbide precipitates at grain boundaries. The preferential corrosion and cracking at grain boundaries can be related to the continuously distributed film-like precipitates along the boundaries. According to the references [9–15], these film-like precipitates are Cr-rich MC-type carbides during heat treatment. When large amounts of MC-type carbides precipitate at grain boundaries, Cr-depleted zones can develop in the adjacent regions, thereby significantly reducing the corrosion resistance of these regions.

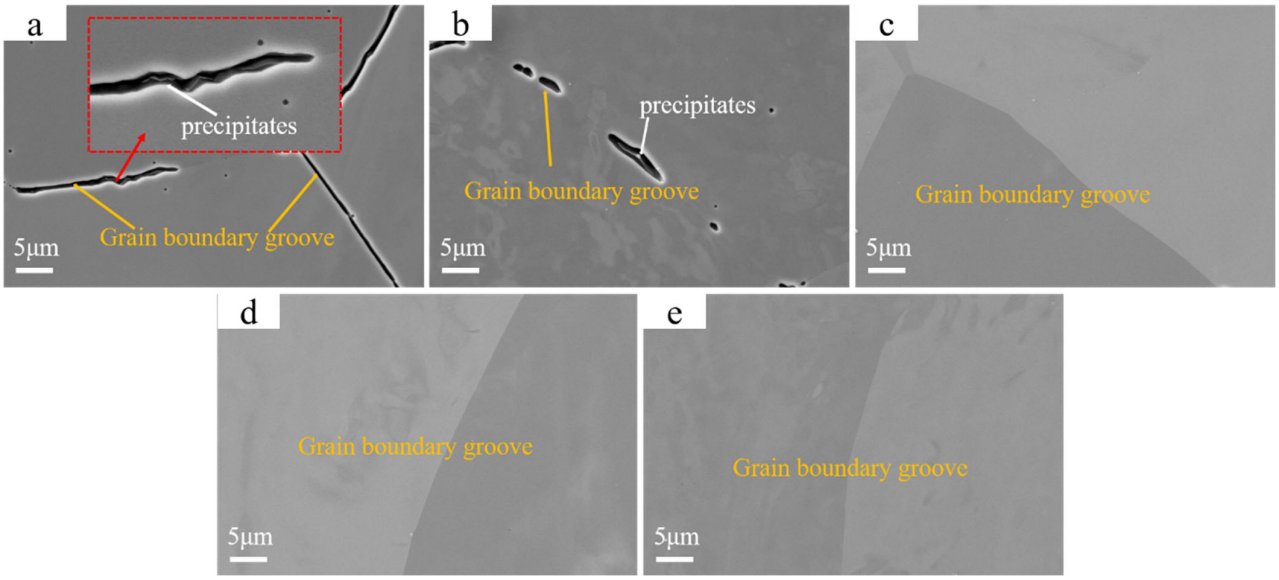

Figure 2. (**a**–**e**) SEM characterization of grain boundary precipitation features in S0Al–S4Al samples after annealing at 800 °C for 1 h. The red dashed box inset in (**a**) is a locally magnified view of the grain boundary.

To further investigate the effect of heat treatment temperature on such precipitates and the temperature dependence of the inhibitory effect of Al, the S0Al and S4Al alloys were annealed at 900 °C and 1000 °C for 1 h, respectively. Their microstructural changes were then examined after etching for the same time, as shown in Figure 4. After annealing

at 900 °C, grain boundary grooves in the S0Al alloy became more obvious. The inset in Figure 4a shows that the film-like precipitates almost continuously covered the entire grain boundaries. After annealing at 1000 °C, the continuous distribution of film-like precipitates along the grain boundaries became even more conspicuous. In contrast, after annealing at 900 °C, the S4Al alloy showed much less grain boundary grooves, and only a small number of precipitates were observed. However, when the annealing temperature was increased to 1000 °C, obvious grain boundary grooves also appeared in the S4Al alloy, together with a large number of film-like precipitates continuously distributed along the grain boundaries. These results confirmed that Al has a clear inhibitory effect on the film-like MC precipitate formation at the grain boundary, and that this effect becomes weaker as the annealing temperature increases.

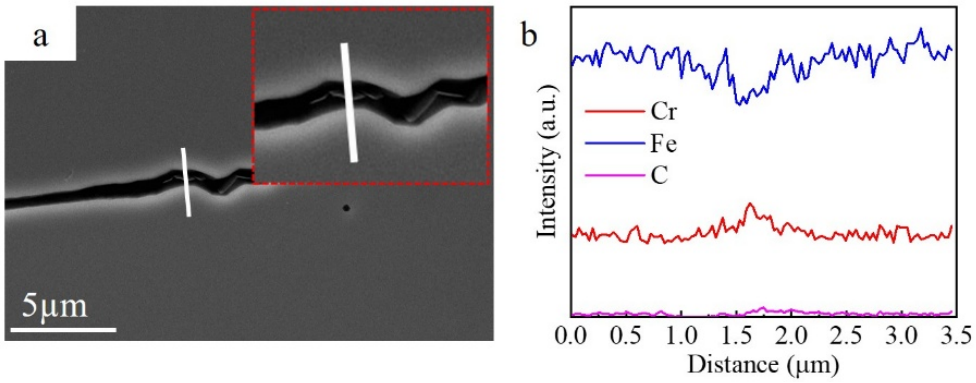

Figure 3. (**a**) SEM image and (**b**) EDS line scan results of grain boundary precipitation characteristics of S0Al sample after annealing at 800 °C for 1 h.

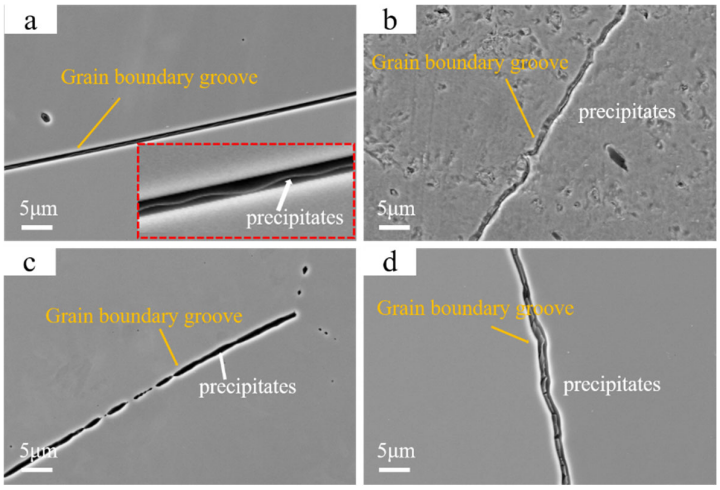

Figure 4. (**a**,**b**) SEM images of the S0Al sample after annealing at 900 °C and 1000 °C; (**c**,**d**) SEM images of the S4Al sample after annealing at 900 °C and 1000 °C. The inset in the red dashed box is a locally magnified view of the grain boundary in (**a**).

Because the etching process may cause partial detachment of the film-like precipitates, and because of the limited resolution of SEM, it is difficult to accurately characterize the morphology and composition of nanoscale precipitates. To further confirm the film-like precipitates' morphological structure and composition at the grain boundary, TEM observations were carried out on the S4Al alloy annealed at 800 °C for 1 h, as well as on the S0Al and S4Al alloys annealed at 1000 °C for 1 h. The results are shown in Figure 5.

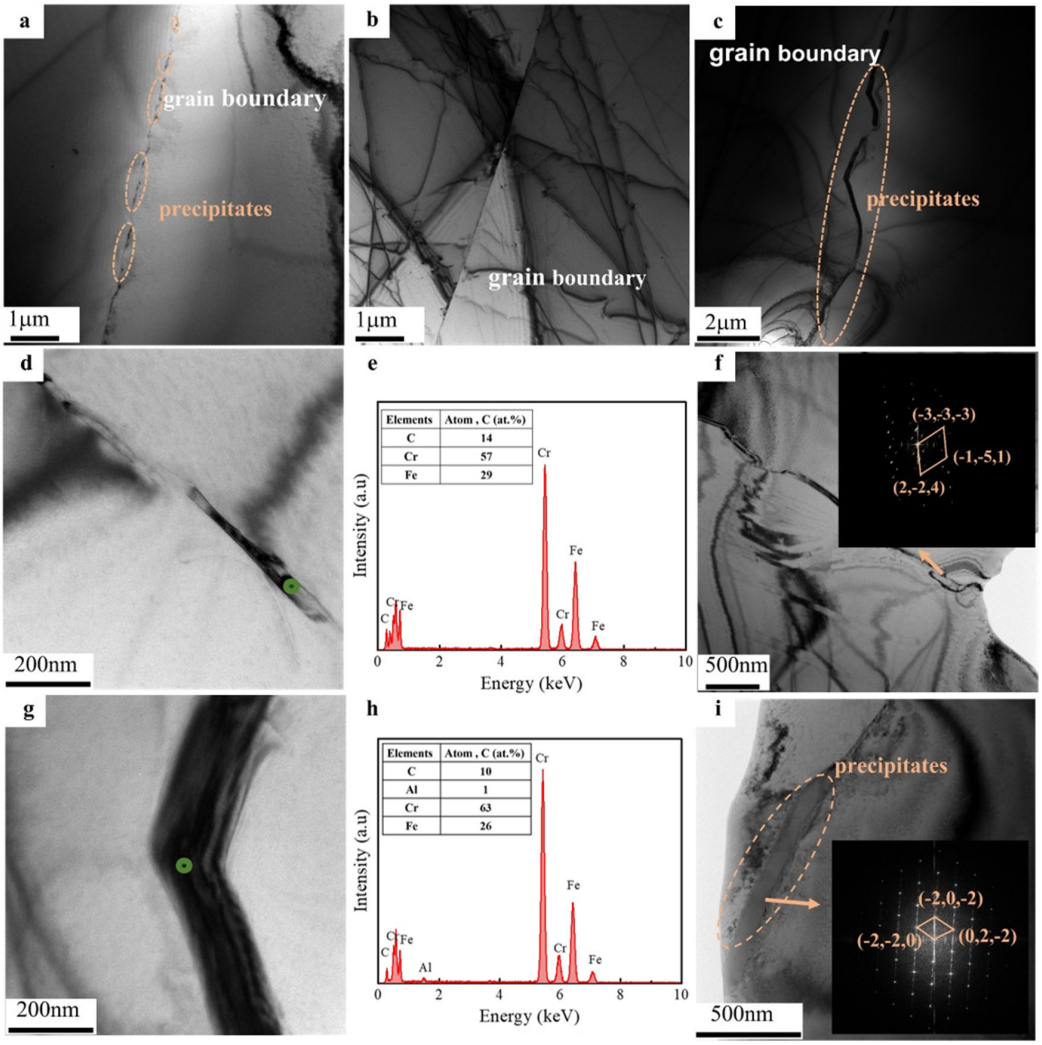

Figure 5. (**a**) Bright-field TEM image of the S0Al sample annealed at 1000 °C for 1 h. (**b**) Bright-field TEM image of the S4Al sample annealed at 800 °C for 1 h. (**c**) Bright-field TEM image of the S4Al sample annealed at 1000 °C for 1 h. (**d**) High-magnification bright-field TEM image of a typical grain boundary precipitate in the S0Al-1000 °C condition (analysis point marked in the image). (**e**) TEM-EDS spectrum acquired from the precipitate marked by the green circle in (**d**). (**f**) Bright-field TEM image of the S0Al sample annealed at 1000 °C for 1 h and the corresponding SAED pattern (indexed reflections are labeled in the inset). (**g**) High-magnification bright-field TEM image of a representative grain boundary precipitate in the S4Al-1000 °C condition (analysis point marked in the image). (**h**) TEM-EDS spectrum acquired from the precipitate marked by the green circle in (**g**). (**i**) Bright-field TEM image of the S4Al sample annealed at 1000 °C for 1 h and the corresponding SAED pattern (indexed reflections are labeled in the inset).

As shown in Figure 5a, after annealing at 1000 °C, a large number of precipitates were observed along the grain boundaries in the S0Al alloy. At higher magnification (Figure 5d), TEM-EDS analysis was performed at the location marked by the green circle in Figure 5d, and the result is presented in Figure 5e. The EDS spectrum shows that the precipitate is highly enriched in Cr, with an atomic fraction of 57 at.%, together with 14 at.% C. This indicates that the grain boundary precipitates are Cr-rich carbides, which also explains the grain boundary cracking observed by SEM after etching. Selected-area electron diffraction (SAED) was further used to analyze the crystal structure of the grain boundary precipitates in the S0Al alloy after annealing at 1000 °C, as shown in Figure 5f. The inset in Figure 5f shows the SAED pattern of the precipitate at the grain boundary. Analysis of the diffraction spots identified three sets of crystal planes, namely (−3, −3, −3), (−1, −5, 1), and (2, −2,

4), along the [−3 1 2] zone axis, indicating that the precipitate has an $M_{23}C_6$-type structure. Combined with the EDS results, it can be confirmed that the grain boundary precipitate in the S0Al alloy is $(Fe, Cr)_{23}C_6$.

Figure 5b shows the grain boundary structure of the S4Al alloy after annealing at 800 °C. Consistent with the SEM observations, the grain boundaries remained clean and no obvious precipitates were observed. This indicates that the addition of Al has a clear inhibitory effect on the formation of $M_{23}C_6$ carbides at grain boundaries in Fe-Cr alloys. Figure 5c shows the grain boundary structure of the S4Al alloy after annealing at 1000 °C, where a large number of precipitates can be seen along the grain boundaries. The composition of these precipitates was further analyzed by TEM-EDS at high magnification. TEM-EDS point analysis was carried out at the region marked by the green circle in Figure 5g, and the result is shown in Figure 5h. The EDS spectrum indicates that the grain boundary precipitates in S4Al after annealing at 1000 °C were still Cr-rich carbides. SAED was also used to analyze the crystal structure of the grain boundary precipitates in the S4Al alloy after annealing at 1000 °C, as shown in the inset of Figure 5i. Analysis of the diffraction pattern identified three sets of crystal planes, namely (−2, 0, −2), (−2, −2, 0), and (0, 2, −2), which can be indexed as the diffraction features of $M_{23}C_6$ along the [−1 1 1] zone axis. Based on the combined EDS and SAED results, it can be concluded that the grain boundary precipitates in the S4Al alloy after annealing at 1000 °C are also $M_{23}C_6$-type Cr-rich carbides.

The microstructural characterization results show that the addition of Al to Fe-15Cr alloy can suppress the precipitation of $M_{23}C_6$ in grain boundaries under low-temperature treatment, which is attributed to the reduced diffusivity of C in BCC iron caused by Al [22–26]. However, annealing at 1000 °C increases the diffusion fluxes of both Cr and C atoms and accelerates their diffusion and segregation to grain boundaries, which act as high-energy sinks. As a result, grain boundary segregation and precipitation occur more readily [9–14,17,18]. Therefore, although the addition of Al cannot completely prevent the formation of $M_{23}C_6$ at the grain boundary, it can significantly delay its precipitation.

3.2. IF-Temperature Spectrum

The IF-temperature spectra of the S0Al-S4Al alloys after annealing at 800 °C are shown in Figure 6. For the S0Al alloy, three IF peaks were detected at about 590 °C, 680 °C, and 770 °C, and were labeled P_Z, P_G, and P_1, respectively. For the S1Al–S4Al alloys, only two IF peaks were observed at around 590 °C and 680 °C. It is worth noting, however, that among the S0Al-S4Al alloys, the P_G IF peak was the lowest in the S0Al alloy and the second lowest in the S1Al alloy.

Many studies have reported the temperature dependence of IF in Fe-based damping alloys [27–31]. In pure Fe, the grain boundary relaxation peak appears at about 0.45 *T*m (*T*m is the melting temperature), and its activation energy is 2.01 eV [30]. Binary Fe-Cr alloys exhibit both a Zener IF peak and a grain boundary IF peak [31,32].

The P_Z peak shifted to a higher temperature as the frequency increased. This is a characteristic feature of a typical Zener internal friction peak arising from the stress-induced reorientation of Cr-Cr solute atom pairs [25,33]. The P_G IF peak at 680 °C shifts to higher temperatures with increasing frequency and shows clear frequency dispersion, suggesting that it is a grain boundary IF peak associated with grain boundary sliding under applied stress. The temperature position of the P_1 peak also remained unchanged with frequency, while the modulus decreased. Figure 6f shows the IF-temperature spectrum of the S0Al sample after annealing at 800 °C for 1 h followed by water quenching. Compared with the furnace-cooled S0Al sample (Figure 6a), the P_1 peak temperature increases after water quenching. Nevertheless, Figure 6f shows that the grain boundaries are already pinned

by precipitates, indicating that precipitation occurred during the 800 °C annealing process. By contrast, the slightly lower P_1 peak temperature observed in Figure 6a may result from the formation of a greater number of precipitates during furnace cooling. Alvise Miotti Bettanini [34] reported that $M_{23}C_6$ carbides dissolve during heating in Fe-11Cr-0.06C stainless steel, and their Thermo-Calc calculation gave an $M_{23}C_6$ dissolution temperature of 816 °C. Their dilatometry and DICTRA results also showed that the dissolution of $M_{23}C_6$ is a thermally activated process and is strongly affected by heating conditions and carbide size. These results suggest that the P_1 peak is likely associated with the interaction between film-like $M_{23}C_6$ precipitates and grain boundaries.

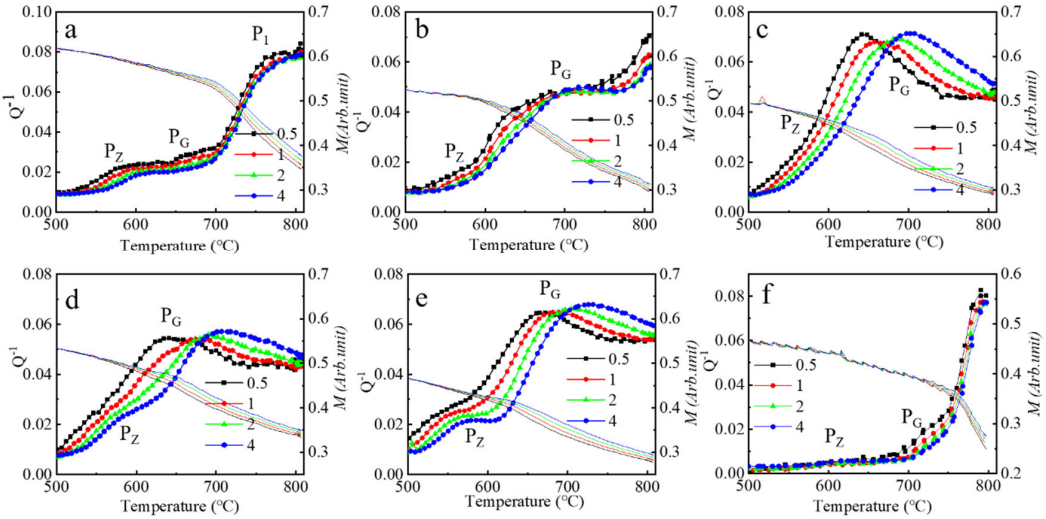

Figure 6. (**a**–**e**) Temperature-dependent IF heating curves of the S0Al-S4Al samples measured after annealing at 800 °C for 1 h and furnace cooling. (**f**) Temperature-dependent IF heating curves of the S0Al sample measured after annealing at 800 °C for 1 h and water quenching.

Grain boundary IF peaks are usually affected by factors such as solute atoms and precipitates [27–31]. In conjunction with the microstructural observations presented in Section 3.1, the IF results indicate that the presence of $M_{23}C_6$-type carbides at the grain boundaries can pin the grain boundaries and impede grain boundary sliding under external stress, thereby suppressing the associated relaxation process induced by grain boundary sliding. When thin film-like $M_{23}C_6$ carbides are continuously distributed along the grain boundaries, grain boundary sliding is markedly suppressed, leading to a grain boundary IF peak with low intensity and a broad, flat profile.

Similar phenomena have also been reported in other metallic systems. For example, studies on grain boundary IF in polycrystalline pure Al with different impurity contents identified a pure grain boundary peak (PM) and a solid-solution grain boundary peak (SS) [29]. When 1.2 wt.% Cu was added to pure Al, a precipitation grain-boundary peak caused by grain-boundary precipitates was observed. Compared with the PM and SS peaks, the precipitation grain-boundary peak showed both a lower peak height and a lower peak temperature. This was attributed to the increased number of precipitate particles, which reduced both the relaxation time and the relaxation strength [29]. In the present study, however, the PM and SS peaks exhibit a complex superposition, giving rise to a grain boundary IF peak with low intensity and a broad, flat profile in the S0Al and S1Al alloys.

3.3. IF-Amplitude Spectrum

The IF-amplitude spectrum is one of the key indicators for evaluating the damping performance of an alloy. Figure 7 shows the IF-amplitude spectra of the S0Al-S4Al alloys after annealing at 800 °C. For all the alloys, the IF value increased rapidly with increasing

amplitude at first, and then decreased gradually after reaching a maximum value. This amplitude peak is a typical feature of magnetomechanical damping for soft ferromagnetic damping alloys [2,5,6]. In addition, the Al-containing alloys reached Q_{max}^{-1} at a lower strain amplitude.

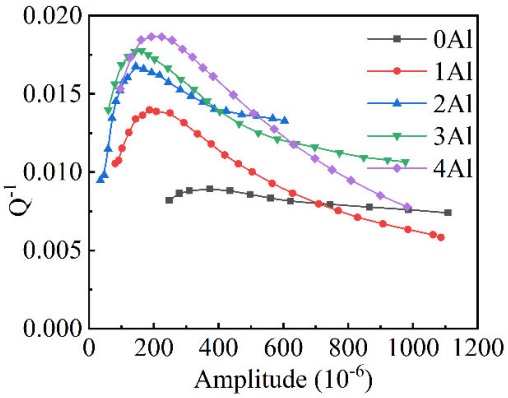

Figure 7. Amplitude-dependent IF curves of the S0Al-S4Al samples after annealing at 800 °C.

The variation of the maximum damping value (Q_{max}^{-1}) with Al content is shown in Figure 8. As the Al content increased, the Q_{max}^{-1} increased monotonically. However, the increase in peak height Q_{max}^{-1} is not in a linear relationship with the Al content. The increasing effect of aluminum content on the peak height gradually weakens when the Al content exceeds 2 wt.%.

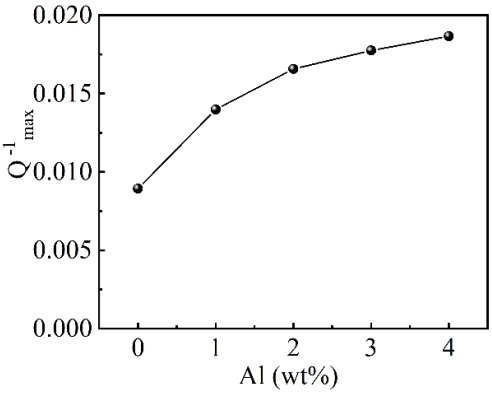

Figure 8. The variation of Q_{max}^{-1} with the Al content.

To investigate the effect of Al content on the damping behavior of the alloy, the S-B phenomenological model was employed. The value of Q^{-1} at low strain amplitude can be expressed as:

$$Q^{-1} = \frac{4\kappa E^2 \lambda_s \gamma}{3\pi\sigma_i^2} \quad (1)$$

where κ is a dimensionless constant, λ_s is the saturation magnetostriction coefficient, E is Young's modulus, γ is the strain amplitude and σ_i is the internal stress. As can be seen from Equation (1), the damping value of the alloy is proportional to the strain amplitude, which is in good agreement with the results obtained in the low-strain-amplitude region of the present study. By differentiating Equation (1) with respect to γ, the Rayleigh slope (S_R) can be obtained as:

$$\frac{dQ^{-1}}{d\gamma} = \frac{4\kappa E^2 \lambda_s}{3\pi\sigma_i^2} = S_R \quad (2)$$

Equations (1) and (2) show that increasing λ_s or decreasing σ_i can improve the damping capacity of the alloy and increase S_R. Previous studies have demonstrated that the addition of Al to Fe-Cr alloys enhances λ_s. Therefore, within the Al content range examined in the present study, the damping capacity increased with increasing Al content, and Q_{max}^{-1} was attained at a lower strain amplitude.

Combined with the microstructural analysis in Section 3.1, it can be seen that continuously distributed $M_{23}C_6$-type carbides were present along the grain boundaries in the S0Al alloy. On the one hand, these precipitates pinned the grain boundaries and suppressed grain boundary relaxation. On the other hand, they acted as additional pinning sites that hinder magnetic domain wall motion, thereby suppressing the damping capacity. As a result, the S0Al alloy exhibited a relatively low Q_{max}^{-1} [21]. After adding 1 wt.% Al, the amount of $M_{23}C_6$ carbide precipitated at the grain boundaries decreased significantly. Although some precipitates were still present, their pinning effect on magnetic domain wall motion was clearly weakened. Therefore, the Q_{max}^{-1} value of the S1Al alloy increased markedly. When the Al content was increased to 2 wt.%, the amount of grain boundary precipitates decreased further, and the hindering effect of grain boundary $M_{23}C_6$ carbides on magnetic domain wall motion was nearly eliminated. As a result, the Q_{max}^{-1} value of the S2Al alloy increased significantly further. For the S2Al-S4Al alloys, since no obvious precipitates were observed at the grain boundaries, the further increase in the Q_{max}^{-1} with increasing Al content mainly arose from the increase in the magnetostrictive effect itself, and the improvement was therefore relatively limited.

3.4. Mechanical Properties of the Alloys

The stress–strain curves of the S0Al-S4Al samples after annealing at 800 °C are shown in Figure 9. All samples exhibited obvious work hardening after yielding, followed by necking and final fracture after reaching the ultimate tensile strength (UTS). Among them, the S0Al alloy showed the lowest UTS, at 278 MPa, with a fracture elongation of up to 56.8%. As the Al content increased, the UTS gradually increased. Compared with S0Al, the UTS of the S4Al alloy increased by 34%, reaching 374 MPa. This improvement is related, on the one hand, to the smaller grain size of the S4Al alloy compared with the S0Al alloy after annealing at 800 °C (Table 2) [35], and on the other hand, to the solid-solution strengthening effect caused by the dissolution of Al into the BCC Fe-Cr-Al matrix [35–38]. That is to say, the addition of Al elements promotes grain refinement and enhances the UTS of the alloy. It is worth noting that the fracture elongation gradually decreased from the S0Al to the S3Al alloy, but increased again to 47.7% in the S4Al alloy. The non-monotonic elongation behavior may be related to the competition between strengthening and plastic strain accommodation. Al addition increases the UTS mainly through solid-solution strengthening and grain refinement. The S4Al alloy contains relatively clean grain boundaries and some coarse grains after annealing at 800 °C (seen in Figures 1 and 2). The clean grain boundaries reduce the tendency for grain-boundary embrittlement, and the coarse grains may reduce the density of grain boundaries acting as barriers to dislocation motion, and thus facilitate dislocation-mediated plastic deformation and plastic strain accommodation [39]. An in situ SEM–EBSD study on Fe-Cr-Al alloys has shown that tensile deformation is closely associated with slip-band formation, crystallographic rotation, orientation-dependent lattice distortion, and local strain heterogeneity [40]. Therefore, the higher elongation of S4Al compared with S3Al may be tentatively attributed to improved plastic strain accommodation.

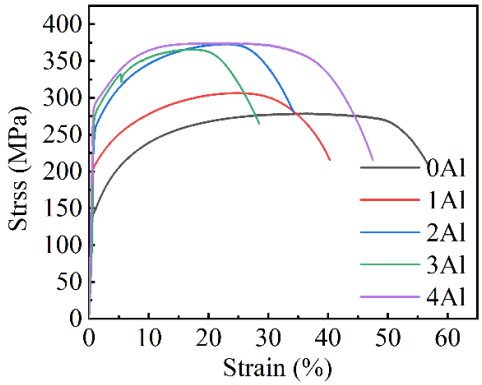

Figure 9. The stress–strain curves of the S0Al-S4Al samples after annealing at 800 °C.

To investigate the effect of annealing temperature on the mechanical properties, the stress–strain curves of the S0Al and S4Al alloys after annealing at 1000 °C were further measured, as shown in Figure 10. Compared with the results after annealing at 800 °C, the UTS values of the S0Al and S4Al alloys after annealing at 1000 °C decreased. It is worth noting that the fracture elongation also decreased markedly to 26.7% and 26.0%, respectively. The decrease in strength is mainly related to grain coarsening (Table 2) [38], whereas the significant reduction in fracture elongation can mainly be associated with grain boundary embrittlement caused by the continuous precipitation of $M_{23}C_6$-type carbides along the grain boundaries [16,19,20], seen in Figures 2 and 4.

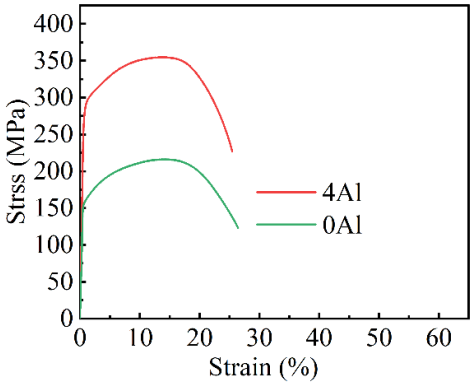

Figure 10. The stress–strain curves of the S0Al and S4Al alloys after annealing at 1000 °C.

4. Conclusions

The study investigated the effects of Al addition and annealing temperature on the microstructure, IF, and mechanical properties of Fe-15Cr-based damping alloys. Al content and annealing temperature remarkably influence the precipitation characteristics of $M_{23}C_6$ at the grain boundary and further affect the IF behavior and mechanical properties of the alloys. After annealing at 800 °C, the Fe-15Cr-S4Al alloy exhibited a good combination of damping performance and mechanical properties. The main conclusions are as follows:

(1) When the heat-treatment temperature is about 800 °C, the addition of Al effectively suppresses the $M_{23}C_6$-type carbide precipitation at the grain boundaries. The S4Al alloy showed a 34% higher strength than S0Al while maintaining a fracture elongation of 47.7%, and the mechanism should also be attributed to grain-refinement and solid-solution strengthening.

(2) When the heat-treatment temperature is about 1000 °C, the suppressing effect of Al on grain boundary carbide precipitation becomes weak, film-like precipitate continue at the grain boundary.

(3) Continuously distributed M23C6-type carbides exerted a significant pinning effect on grain boundaries, suppressing grain boundary relaxation and reducing damping capacity.
(4) The addition of Al improved the room temperature damping performance of the alloys.

Author Contributions: Conceptualization, W.J.; Methodology, X.W., W.J. and M.S.; Validation, Y.S.; Formal analysis, H.Z.; Investigation, Y.J.; Data curation, Y.S.; Writing—original draft, Y.S.; Writing—review & editing, W.J. and M.S.; Project administration, W.J. and M.S. All authors have read and agreed to the published version of the manuscript.

Funding: This work is supported by the Anhui Provincial Natural Science Foundation (Grant Nos. 2508085ME119, 2408085ME128).

Data Availability Statement: Data will be made available on request.

Conflicts of Interest: The authors declare no conflict of interest.

References

1. Pulino-Sagradi, D.; Sagradi, M.; Karimi, A.; Martin, J.L. Damping capacity of Fe-Cr-X high-damping alloys and its dependence on magnetic domain structure. *Scr. Mater.* **1998**, *39*, 131–138. [CrossRef]
2. Azcoïtia Ch Karimi, A. Magnetomechanical damping in Fe-Cr alloys and effect of Al and Mo addition. *J. Alloys Compd.* **2000**, *310*, 160–164. [CrossRef]
3. Jiang, G.; Xu, D.; Feng, P.; Guo, S.; Yang, J.; Li, Y. Corrosion of FeCrAl alloys used as fuel cladding in nuclear reactors. *J. Alloys Compd.* **2021**, *869*, 159235. [CrossRef]
4. Xu, Y.; Chen, X. On relationship between annealing treatment and magnetostriction behavior of Fe–16Cr–2.5Mo damping alloy. *J. Alloys Compd.* **2014**, *582*, 364–368. [CrossRef]
5. Karimi, A.; Azcoitia, C.; Degauque, J. Relationships between magnetomechanical damping and magnetic properties of Fe–Cr(Al,Mo) alloys. *J. Magn. Magn. Mater.* **2000**, *215–216*, 601–603. [CrossRef]
6. Wang, H.; Tian, X.F.; Yin, C.; Huang, Z. The effect of heat treatment and grain size on magnetomechanical damping properties of Fe–13Cr–2Al–1Si alloy. *Mater. Sci. Eng. A* **2014**, *619*, 199–204. [CrossRef]
7. Chen, K.; Yan, J.; Li, N.; Luo, M.; Shi, H.; Zhu, X.; Liu, Y.; Zhao, X.; Zhang, R. The effect of the annealing temperature on the damping capacity under constant prestress, mechanical properties and microstructure of an Fe–11Cr-2.5Mo-0.1Zr-1.0Ni forged damping alloy. *J. Alloys Compd.* **2020**, *815*, 152429. [CrossRef]
8. Xu, Y.-g.; Chen, X.-g.; Yang, Z.; Zhang, S. Attenuation of magnetomechanical hysteresis effect by excessively annealing Fe-16Cr-2.5~3.5Mo damping alloys. *J. Magn. Magn. Mater.* **2022**, *563*, 169870. [CrossRef]
9. Wang, B.; Li, Y.; Li, H.; Zhao, G.; Song, Y.; Xu, H. Influence of homogenized annealing on the intergranular corrosion behavior of super ferritic stainless steel S44660. *Corros. Sci.* **2025**, *247*, 112783. [CrossRef]
10. Huang, X.; Wang, D.; Yang, Y. Effect of precipitation on intergranular corrosion resistance of 430 ferritic stainless steel. *J. Iron Steel Res. Int.* **2015**, *22*, 1062–1068. [CrossRef]
11. Qu, H.P.; Lang, Y.P.; Chen, H.T.; Rong, F.; Kang, X.F.; Yang, C.Q.; Qin, H.B. The effect of precipitation on microstructure, mechanic properties and corrosion resistance of two UNS S44660 ferritic stainless steels. *Mater. Sci. Eng. A* **2012**, *534*, 436–445. [CrossRef]
12. Kaneko, K.; Fukunaga, T.; Yamada, K.; Nakada, N.; Kikuchi, M.; Saghi, Z.; Barnard, J.S.; Midgley, P.A. Formation of M23C6-type precipitates and chromium-depleted zones in austenite stainless steel. *Scr. Mater.* **2011**, *65*, 509–512. [CrossRef]
13. Mizouchi, M.; Yamazaki, Y.; Iijima, Y.; Arioka, K. Low temperature grain boundary diffusion of chromium in SUS316 and 316L stainless steels. *Mater. Trans.* **2004**, *45*, 2945–2950. [CrossRef]
14. Sahu, S.; Patel, S.K.; Shekhar, S. The effect of grain boundary structure on chromium carbide precipitation in alloy 600. *Mater. Chem. Phys.* **2021**, *260*, 124145. [CrossRef]
15. Aydoğdu, G.H.; Aydinol, M.K. Determination of susceptibility to intergranular corrosion and electrochemical reactivation behaviour of AISI 316L type stainless steel. *Corros. Sci.* **2006**, *48*, 3565–3583. [CrossRef]
16. Ren, W.; Wang, L. Precipitation behavior of M23C6 in high nitrogen austenitic heat-resistant steel. *J. Alloys Compd.* **2022**, *905*, 164013. [CrossRef]
17. Mishin, Y. Solute drag and dynamic phase transformations in moving grain boundaries. *Acta Mater.* **2019**, *179*, 383–395. [CrossRef]
18. Kim, S.G.; Park, Y.B. Grain boundary segregation, solute drag and abnormal grain growth. *Acta Mater.* **2008**, *56*, 3739–3753. [CrossRef]
19. Peng, B.; Zhang, H.; Hong, J.; Gao, J.; Wang, Q.; Zhang, H. Effect of aging on the impact toughness of 25Cr–20Ni–Nb–N steel. *Mater. Sci. Eng. A* **2010**, *527*, 1957–1961. [CrossRef]

20. Zheng, L.; Hu, X.; Kang, X.; Li, D. Precipitation of M23C6 and its effect on tensile properties of 0.3C–20Cr–11Mn–1Mo–0.35N steel. *Mater. Des.* **2015**, *78*, 42–50. [CrossRef]
21. Wang, W.; Zhou, B. The correlation of damping capacity with grain-boundary precipitates in Fe-Cr-based damping alloys annealed at high temperature. *Mater. Sci. Eng. A* **2004**, *366*, 45–49. [CrossRef]
22. Huang, L.; Eyméoud, P.; Maugis, P. Atomistic investigation on the impact of substitutional Al and Si atoms on the carbon kinetics in ferrite. *J. Alloys Compd.* **2022**, *921*, 166031. [CrossRef]
23. Strahl, A.; Golovin, I.S.; Neuhäuser, H.; Golovina, S.B.; Sinning, H.R. Influence of Al concentration on the short-range and long-range diffusion of carbon in Fe-Al alloys. *Mater. Sci. Eng. A* **2006**, *442*, 128–132. [CrossRef]
24. Golovin, I.S.; Golovina, S.B. Effect of alloying α-Fe with aluminum, silicon, cobalt, and germanium on the snoek relaxation parameters. *Phys. Met. Metallogr.* **2006**, *102*, 593–603. [CrossRef]
25. Golovin, I.S.; Jäger, S.; Semin, V.A.; Serzhantova, G.V.; Sinning, H.R.; Sokolova, O.A.; Stein, F.; Golovin, S. Snoek-type and Zener relaxation in Fe-Si-Al alloys. *Solid State Phenom.* **2008**, *137*, 69–82. [CrossRef]
26. Liu, P.; Xing, W.; Cheng, X.; Li, D.; Li, Y.; Chen, X.Q. Effects of dilute substitutional solutes on interstitial carbon in α-Fe: Interactions and associated carbon diffusion from first-principles calculations. *Phys. Rev. B* **2014**, *90*, 024103. [CrossRef]
27. Mari, D. The contribution of mechanical spectroscopy to understanding grain boundary sliding. *Mater. Res.* **2018**, *21*, e20180369. [CrossRef]
28. Mishin, Y.; Suzuki, A.; Uberuaga, B.P.; Voter, A.F. Stick-slip behavior of grain boundaries studied by accelerated molecular dynamics. *Phys. Rev. B* **2007**, *75*, 224101. [CrossRef]
29. Kê, T.S.; Cui, P. Effect of solute atoms and precipitated particles on the optimum temperature of the grain boundary internal friction peak in aluminium. *Scr. Metall. Mater.* **1992**, *26*, 1487–1492. [CrossRef]
30. Sun, M.; Jiang, W.; Liu, X.; Chen, T.; Wang, X.; Fang, Q. A comparative study on the grain boundary internal friction peak of pure iron. *Mater. Lett.* **2021**, *305*, 130814. [CrossRef]
31. Barrand, P. Grain boundary relaxations in iron-chromium alloys. *Acta Metall.* **1966**, *14*, 1247–1256. [CrossRef]
32. De Batist, R. Internal friction of iron-chromium alloys in the temperature range between 20 and 800 °C. *J. Nucl. Mater.* **1969**, *31*, 307–315. [CrossRef]
33. Hirscher, M.; Brossmann, U.; Henes, R. Measurement of the Zener relaxation in high-purity FeCr single crystals. *Mater. Trans. JIM* **2000**, *41*, 82–86. [CrossRef]
34. Miotti Bettanini, A.; Ding, L.; Mithieux, J.-D.; Parrens, C.; Idrissi, H.; Schryvers, D.; Delannay, L.; Pardoen, T.; Jacques, P.J. Influence of M23C6 dissolution on the kinetics of ferrite to austenite transformation in Fe-11Cr-0.06C stainless steel. *Mater. Des.* **2019**, *162*, 362–374. [CrossRef]
35. Ukai, S.; Yano, Y.; Inoue, T.; Sowa, T. Solid-solution strengthening by Al and Cr in FeCrAl oxide-dispersion-strengthened alloys. *Mater. Sci. Eng. A* **2021**, *812*, 141076. [CrossRef]
36. Springer, H.; Baron, C.; Tanure, L.; Rohwerder, M. A combinatorial study of the effect of Al and Cr additions on the mechanical, physical and corrosion properties of Fe. *Mater. Today Commun.* **2021**, *29*, 102947. [CrossRef]
37. Du, L.Y.; Lu, H.H.; Xing, Z.Z.; Han, J.S.; Zhang, S.H.; Li, J.C. Effects of Al additions on precipitation, recrystallization and mechanical properties of hot-rolled ultra-super ferritic stainless steels. *J. Mater. Res. Technol.* **2023**, *27*, 4278–4289. [CrossRef]
38. Hansen, N. Hall-Petch relation and boundary strengthening. *Scr. Mater.* **2004**, *51*, 801–806. [CrossRef]
39. Ding, R.; Wang, H.; Jiang, Y.; Liu, R.; Jing, K.; Sun, M.; Zhang, R.; Qiu, S.; Xie, Z.; Deng, H.; et al. Effects of ZrC addition on the microstructure and mechanical properties of Fe-Cr-Al alloys fabricated by spark plasma sintering. *J. Alloys Compd.* **2019**, *805*, 1025–1033. [CrossRef]
40. Bibhanshu, N.; Gussev, M.N.; Massey, C.P.; Field, K.G. Investigation of deformation mechanisms in an advanced FeCrAl alloy using in-situ SEM-EBSD testing. *Mater. Sci. Eng. A* **2022**, *832*, 142373. [CrossRef]

Disclaimer/Publisher's Note: The statements, opinions and data contained in all publications are solely those of the individual author(s) and contributor(s) and not of MDPI and/or the editor(s). MDPI and/or the editor(s) disclaim responsibility for any injury to people or property resulting from any ideas, methods, instructions or products referred to in the content.